Ocean Engineering 365 (2026) 127157

Contents lists available at ScienceDirect

Ocean Engineering

journal homepage: www.elsevier.com/locate/oceaneng

Research paper

Power performance and loads characterization of laboratory-scale cross-flow rotors fabricated using additive manufacturing

James R. McVey [a,*], Abigale C. Snortland [a], Christopher R. Rumple [b], John T. Zaengle [c], Robert J. Cavagnaro [b], Michelle D. Fenn [c], Gregory Talpey [d], Emma N. Geon [b]

[a] Pacific Northwest National Laboratory, Seattle, WA, 98109, United States
[b] Pacific Northwest National Laboratory, Sequim, WA, 98382, United States
[c] Pacific Northwest National Laboratory, Richland, WA, 99354, United States
[d] Department of Mechanical Engineering, University of Washington, Seattle, WA, 98195, United States

ARTICLE INFO

Keywords:
Cross-flow rotor
Marine renewable energy
Additive manufacturing

ABSTRACT

Tidal energy conversion is a relatively new application for additive manufacturing (AM), where the focus has been on fabricating axial-flow turbine blades. AM techniques add material precisely where it is needed, creating more complex shapes with less waste. Cross-flow rotor geometry presents an opportunity for AM to improve rotor performance by fabricating features that cannot be created economically via conventional manufacturing. The challenges associated with using AM in cross-flow design include water resistance and degradation over time while retaining a level of quality equivalent to conventionally machined parts. In this work, AM materials were tested by environmentally conditioning samples in a seawater tank for 5 months, followed by performance and phase-resolved load testing of laboratory-scale rotors in a hydraulic flume. We found that while metals like titanium and Inconel have excellent performance in marine environments, achieving the desired geometry and performance is difficult. Thermoplastics degraded in seawater but were easier to form into desired geometries and could exceed the performance of an aluminum control rotor. Warping and surface finish were significant detractors from AM rotor performance. These results suggest that the primary benefits of using AM for cross-flow rotors is to quickly fabricate and test unconventional rotor geometries.

1. Introduction

Vertically oriented cross-flow turbines have potential for community-scale and microgrid power applications due to their ability to harvest power from any current direction without the need for a yaw mechanism. While simpler designs are drag-based, the highest performance rotors utilize hydrofoils to generate lift to rotate and generate power. For these turbines, blades are attached to the central shaft by a support structure (Saini and Saini, 2019), typically a flat plate or a strut with a hydrofoil cross-section (Strom et al., 2018). Support structures transmit forces generated by fluid–structure interactions to the central shaft. The blade–strut joint can be prone to failure, as this interface sees significant strain and bending moments (Bichanich et al., 2025) and significantly impacts turbine performance and stability (Strom et al., 2018). Manufacturing blade–strut joints that can provide the necessary stability and durability can be difficult to achieve, especially at an acceptable cost. AM may provide the ability to cost-effectively fabricate cross-flow turbine parts without compromising on strength and power performance.

Additive manufacturing (AM) is finding a niche in many industries through its ability to create complex geometries that are difficult to manufacture conventionally. The use of AM for axial-flow turbine blade fabrication is a current topic of research, building on the traditional method of manufacturing blades using composites (e.g. Murdy et al., 2024b). Gonabadi et al. (2024) investigated the material properties of AM-printed composites and analyzed the structural response of axial-flow rotor blades fabricated with those composites. Their results indicate that AM composite materials are not strong enough to resist the bending moments induced hydrodynamically on the blades. González-Montijo et al. (2023) investigated the use of printing a central spar for axial-flow rotor blades using laser metal deposition, and found the method structurally successful but required surface finishing. Murdy et al. (2024a) found that using AM to create molds and/or individual pieces for axial-flow rotors was more successful than a single-print solution.

* Corresponding author.
E-mail address: james.mcvey@pnnl.gov (J.R. McVey).

https://doi.org/10.1016/j.oceaneng.2026.127157
Received 28 January 2026; Received in revised form 10 July 2026; Accepted 20 July 2026
Available online 29 July 2026

Using AM to produce cross-flow rotors has similar challenges to axial-flow blades, with the additional challenge of creating blade–strut and strut–shaft joints strong enough to handle high fluctuating loads and stress concentrations. Tidal turbines operate in high-energy, turbulent environments that induce significant structural loading and torque fluctuations on the rotor. The highest stresses concentrate at the blade root; for an axial rotor, this is where a blade connects to the central shaft (Liu and Veitch, 2012; Harrold and Ouro, 2019), while for a cross-flow rotor, this is where the blade connects to the support structure(s). Cross-flow rotors, even in laminar flow, experience fluctuating loads from the continuously fluctuating angle of attack and negative flow acceleration through the rotor (Snortland et al., 2025b). The loads resulting from these pressure changes stress the hardware that connects the blade to the struts and the struts to the central shaft (e.g., Bassett et al., 2025). These loads are cyclical in nature and must be considered in design to avoid fatigue failure of the rotor.

Stiffness, surface finish, and service life are additional factors that AM solutions must address. Blade compliance is attributed to reductions in rotor thrust and power (Marone et al., 2025). Rougher surface finishes (Howell et al., 2010; Gonabadi et al., 2024) and marine growth (Stringer and Polagye, 2020) can also dramatically reduce rotor performance. A part's service life, which is directly related to the material used, is critical because is can affect all of the above factors. While many AM thermoplastic materials degrade in the marine environment (Chaudhary et al., 2023), carbon-reinforced composites are particularly susceptible (Dong et al., 2024; Ghabezi et al., 2025; LeBlanc et al., 2024), whereas one thermoplastic material, Ultem 9085, has been shown to resist degradation (LeBlanc et al., 2024; Wang et al., 2024). Murdy et al. (2023) reported environmental degradation of several printed polymer and metal materials after a submersion period of 5 months in a recirculating seawater tank. Their results found significant material property changes occurred in carbon-reinforced thermoplastics while little material degradation was observed in the metal and non-reinforced thermoplastics. In follow-on work, Lusty et al. (2024) analyzed composite material fatigue performance in a modified load frame, where the samples were tested while submerged in synthetic seawater. They found fatigue life was decreased after seawater immersion for the thermoplastics tested.

This work investigates the potential of AM to produce cross-flow rotors that can withstand the marine environment and are comparable to those fabricated with conventional manufacturing techniques in terms of power performance and loads characteristics. First, AM thermoplastics and metal materials were investigated to evaluate their potential for use in cross-flow rotor fabrication. Material properties of the AM materials were then evaluated using samples that underwent environmental conditioning. From these materials, small-scale cross-flow rotors were designed, fabricated, and tested in a laboratory flume to compare performance and loads to that of a conventionally-manufactured aluminum rotor. The print quality of the rotors was also quantified via profilometry and 3D scan measurements. The results presented herein inform researchers and developers to use AM early in the design process to rapidly produce and test various geometries using inexpensive materials, which, later in the design process, can be substituted to more expensive, marine-grade materials without sacrificing performance, saving manufacturing time and costs.

2. Methods

2.1. Material down-selection

With a plethora of AM materials commercially available, the material selection process focused on those that could be suitable for printing small-scale rotors, on the order of 10 cm, and quickly fabricated in-house or from a 3rd party vendor. Material selection analysis focused on fatigue life, strength to weight ratio, corrosion resistance, elastic modulus, water ingress, and cost of material. Six materials were ultimately chosen for experimental evaluation, including Essentium HTN-CF25, Markforged Onyx, Formlabs GreyPro, Formlabs Rigid10k, titanium Ti–6Al–4V, and Inconel 718 (Table 1).

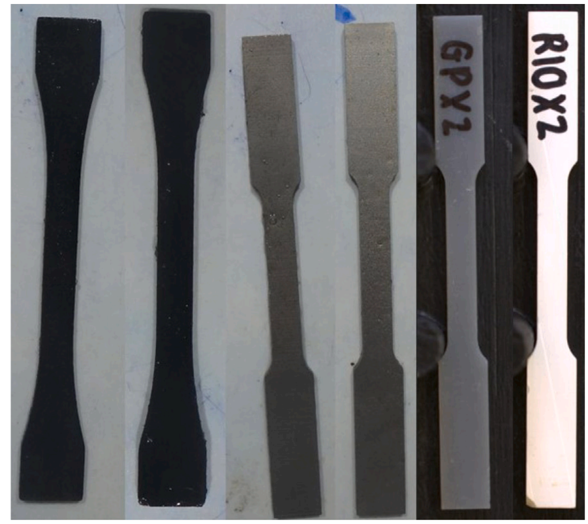

Fig. 1. 3D Printed Dogbone Samples, one of each material. From left to right: Markforged Onyx, Essentium HTN-CF25, Inconel 718, titanium Ti–6Al–4V, Formlabs GreyPro, Formlabs Rigid10k.

The first four materials are thermoplastics, where Essentium and Onyx are carbon-fiber reinforced nylons and the Formlabs materials are proprietary resins. These materials have high strength, toughness, and chemical resistance compared to other plastics, though Essentium and Onyx printed with continuous fiber have been shown to degrade in marine applications (Dong et al., 2024; Ghabezi et al., 2025; LeBlanc et al., 2024). The Essentium and Onyx samples for these tests were printed using a fused deposition modeling (FDM) printer, where the input filament is nylon embedded with chopped carbon fiber. Formlabs GreyPro has similar published material properties to Ultem 9085, one that was not available in-house, while Formlabs Rigid10k is glass-based thermoplastic that is the stiffest material Formlabs offers. The Formlabs printer is a stereolithography apparatus (SLA), where individual layers of resin are cured using a UV laser.

Titanium and Inconel are two metals commonly used in high-performance applications, and can be applied through AM with direct metal laser sintering (DMLS). DMLS is an industrial AM process were a laser is used to sinter material in successive layers of metal powder. These metals were chosen because of their high strength-to-weight ratios and superior corrosion resistance compared to other metals, such as stainless steels and aluminum.

2.2. Environmental conditioning of materials

Tensile testing was first conducted on samples (Fig. 1) created from each material, both using dry samples and those that underwent 5 months of environmental conditioning in a 1.5 m × 1.6 m recirculating seawater tank at Pacific Northwest National Laboratory's (PNNL's) Sequim campus (Fig. 2). The recirculating tank continuously cycles raw seawater from Sequim Bay, fully recirculating every 12 h. This effectively mixes new seawater with the previous 12 h of seawater, muting the diurnal cycles of temperature, salinity, organics, etc, but tracking with the longer-term environmental trends that the Bay experiences. Environmental conditioning focused on analyzing the effects of seawater immersion but not on biofouling.

The sample shapes and tensile tests followed the ISO 527-1 standard (International Organization for Standardization, 2019) for the plastic materials and the ASTM E8 standard (ASTM International, 2021) for the

Table 1
Published material properties.

Material	Print process	Elastic modulus [GPa]	Ultimate tensile strength [MPa]	Density [g/cm^3]
Essentium (Essentium, 2020)	FDM[1]	6.32	74.5	1.32
Onyx (MarkForged, 2020)	FDM[1]	2.4	37	1.2
Ultem 9085 (MarkForged, 2026)	FDM[1]	2.5	68	1.34
GreyPro (Formlabs, 2024a)	SLA[2]	2.6	61	1.2
Rigid10k (Formlabs, 2024b)	SLA[2]	11	81	1.7
Titanium (Protolabs, 2026b)	DMLS[3]	113.8	993	4.43
Inconel (Protolabs, 2026a)	DMLS[3]	200	993	8.19

[1]FDM: Fused Deposition Modeling
[2]SLA: Stereolithography
[3]DMLS: Direct Metal Laser Sintering

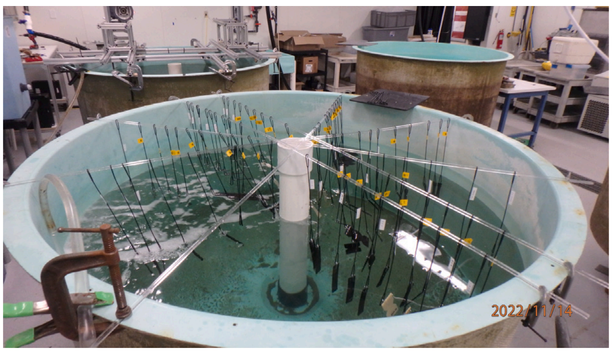

Fig. 2. Test samples in the seawater tank.

metals materials, with the long dimension scaled to 75 and 100 mm, respectively. These tensile tests provided information on the variability in the quality of the prints as well as material degradation after seawater exposure.

Three samples were printed from each material. The carbon-reinforced nylons were printed on a Markforged Mark Two FDM printer with 100% infill, 2 wall layers, and a layer height of 0.1 mm. The Formlabs thermoplastics were printed on a Formlabs Form 3L printer with the manufacturer software's default print settings and a layer height of 0.1 mm. The metal samples were printed by a 3rd party vendor on a GE Additive M2 DMLS printer, layer height of 30 μm. For tensile testing, plastic samples were set up using a 5 kN load cell and a 10 N preload; metal samples were set using a 30 kN load cell and a 13.3 N preload.

For environmental conditioning, sample sets from each material were weighed to the nearest 0.1 g and submerged in seawater for a period of 5 months. Untreated seawater was cycled through the seawater tank, at a rate where the full volume of the tank was exchanged every 12 h. Samples were hung from acrylic rods spanning the top of the tank, protecting them from galvanic corrosion. After conditioning, samples were removed, weighed, and photographed. Samples were wiped clean with a cloth towel, weighed again, and then tensile-tested to obtain the post-conditioning stress–strain curves. This testing was done alongside the National Laboratory of the Rockies (NLR) testing of similar materials, described in Murdy et al. (2023).

2.3. Rotor design

Cross-flow turbine rotors were designed and printed for performance characterization at the Alice C. Tyler Flume at the University of Washington (UW). Two designs were created based on the rotor tested and reported in Hunt et al. (2024). Each rotor had a radius, r, of 8.6 cm, height of 24.1 cm, and blade/strut chord length of 4.06 cm. All AM designs utilized a NACA0018 blade cross-section as well as a thicker strut airfoil cross-section (NACA0012) than the baseline rotor (NACA0008) for improved support. The first rotor design followed Hunt et al. (2024)'s specifications, while the second had a redesigned blade–strut joint. For the former, the blade–strut joint is a 90 degree flush connection, hereafter referred to as the sharp joint. For the latter, the blade and strut joint was lofted similar to an aircraft winglet (hereafter lofted joint), which is more difficult to conventionally manufacture (Fig. 3). In URANS simulations, Villeneuve et al. (2021), showed cross-flow turbines with lofted joints outperformed blade-only simulations, and attributed the performance gains to a reduction in induced drag. Winglets reduce drag on a finite wing by reducing the influence of lift-generated vortices acting on the wingtip, and it is hypothesized here that lofting the joint between the cross-flow blade and strut could, in the same way, smooth out vortices shedding off of the blade–strut interface.

The final shaft-rotor design is shown in Fig. 3 and consisted of the blade(s), the struts, and a shaft-mounting interface on each strut. Holes and slots were printed in the mounting surface for the 1.27 cm diameter steel shaft and shaft mounting collars. These holes needed to be oversized by 5% to handle material expansion during the printing process for all materials. The shaft-mount collars were sized for the 1.27 cm shaft and tapped in two locations for M8 screws to bolt the rotor to the collar. The collars and printed rotor could then be slid onto a commercial-off-the-shelf D-shaft and clamped into place. This design allowed rotors to be installed and removed from the central shafts quickly and effectively for testing.

For each thermoplastic material, one-bladed and two-bladed rotors were printed with each blade–strut joint design. Two-bladed rotors were created for power performance characterization while one-bladed rotors were printed to understand and isolate the forces acting on each blade. Manufacturing metal rotors using DMLS proved challenging and required iteration with the vendor. While one-bladed rotors printed successfully, a critical design change needed to be made for the two-bladed rotor. The trailing edge needed to be "blunted" to provide enough surface for the support structure. Attempts to print a high quality two-bladed rotor were halted after new design iterations produced parts with diminishing returns. Lessons learned from the metal printing process are described in the Appendix. Because of these difficulties, a single one-bladed rotor with the sharp joint was printed and tested in titanium and Inconel, while only a single two-bladed rotor was printed in Inconel.

2.4. Performance testing

UW's Alice C. Tyler Flume is a recirculating water channel powered by two variable-frequency drive pumps capable of achieving flow speeds up to 1.1 m/s. Water flows through a stilling basin with flow straighteners, followed by a free-surface glass test section that is 0.76 m wide by 4.6 m long. Maximum fill depth through the test section is 0.6 m. The turbulence intensity across operating conditions ranges between 1%–3%. The water temperature, which is used to alter the Reynolds number without changing other parameters, is maintained using a pool heater and industrial chiller. Test instrumentation, shown in Fig. 4, included a servomotor to regulate turbine rotation, load cells to measure forces and moments, an acoustic Doppler velocimeter (ADV)

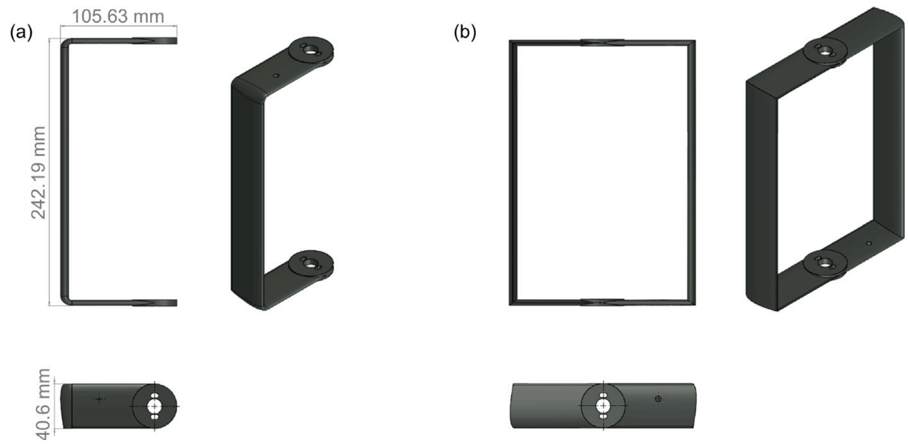

Fig. 3. Small-scale cross-flow turbine drawings. Subplot (a) shows a one-bladed rotor with the lofted blade–strut joint design, and subplot (b) shows the two-bladed rotor with the 90-degree blade–strut design.

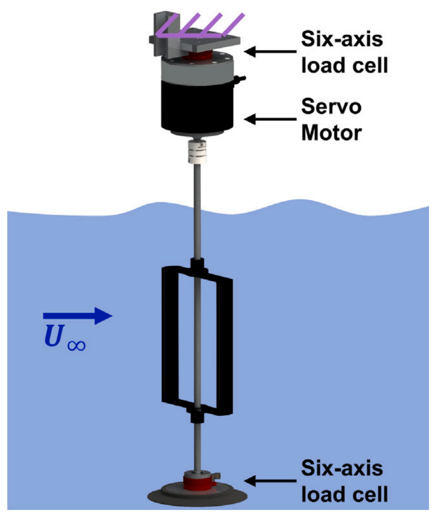

Fig. 4. Performance measurement setup for flume tests. The rotor is set on a shaft, connected with a suction plate to the bottom of the flume and a servo motor above, positioned on a gantry.

Table 2
Target flume conditions.

Condition	1	2	3
Depth [m]	0.55	0.55	0.55
U_∞ [m/s]	0.59	0.82	1.00
Temp. [°C]	35.0	0.82	12.2
Re_d	140,238	140,221	140,085
Blockage	9.92%	9.92%	9.92%
Fr_d	0.254	0.353	0.431

Table 3
Dogbone weight change.

	Dry [g]	Wet [g]	Change [%]
Essentium	1.2	1.3	8.3
Onyx	1.2	1.2	0.0
GreyPro	2.27	2.35	3.66
Rigid10k	3.62	3.68	1.81
Titanium	8.0	8.0	0.0
Inconel	14.5	14.6	0.7

to measure inflow, and ultrasonic free-surface transducers to measure water depth variation. Data from these sensors is streamed to MATLAB via Simulink Desktop Real-Time for processing and analysis.

Each rotor and shaft was oriented vertically in the flume test section. The upper end of the shaft was connected to a servomotor (Yaskawa SGMCS-05BC341) that regulates the rotation rate, ω, and tracks angular position with a high-resolution encoder. Forces and moments acting on the rotor were measured by a pair of 6-axis load cells (ATI Mini45), one at the top of the shaft near the servomotor and one at the bottom of the shaft, which is secured in position using a pneumatic suction plate. A thermal isolation assembly separated the servomotor from the top load cell to reduce thermal drift over the course of experiments. Turbine position and forces were acquired at 1000 Hz in MATLAB using a National Instruments PCIe-6353 data acquisition system. Height of the free surface was measured by an ultrasonic transducer (Omega LVU32) at the flume inlet as the basis for regulating water depth. Inflow velocity to the rotor, U_∞, was measured with the ADV (Nortek Vectrino, 16 Hz sampling rate) at a distance 5 rotor-diameters upstream of the shaft. Inflow conditions were set at three speeds (nominally 0.59, 0.82 and 1.00 m/s). To maintain non-dimensional similarity across the test matrix, the Reynolds and Froude numbers of each inflow condition were held constant by adjusting temperature and water depth. Experimental conditions for each test are provided in Table 2.

Turbine performance and forcing are typically reported as functions of the tip–speed ratio, $\lambda = \frac{r\omega}{U_\infty}$, where r is rotor radius, and θ is the azimuthal blade position. Turbine power, P, is non-dimensionalized as the coefficient of performance defined as

$$C_P = \frac{P}{\frac{1}{2}\rho U_\infty^3 DS}, \quad (1)$$

where D is the turbine diameter based on the outer blade surface and S is the blade-span.

Blade-level forces (force produced by an individual turbine blade) were investigated for the one-bladed rotors. These are computed following the physics-based force decomposition method from Snortland et al. (2025b). This methodology computes the blade-level hydrodynamic force components using force measurements at the turbine center shaft by removing turbine shaft and strut forces while accounting for turbine inertia. In this work, it was not possible to remove the force contribution from the struts since the rotors were printed in one piece. However, forces on the half-struts are anticipated to be minimal in comparison to forces on the blade. The blade-level normal and tangential forces, F_r (normal to the blade path) and F_θ (tangential to the blade path), are non-dimensionalized as

$$C_F = \frac{F}{\frac{1}{2}\rho U_\infty^2 DS}. \quad (2)$$

Table 4
Dogbone elastic moduli.

	Published [GPa]	Dry [GPa] ± SD	Wet [GPa] ± SD	Change [%]
Essentium	6.32	6.00 ± 0.070	2.173 ± 0.168	−63.8
Onyx	2.4	0.867 ± 0.0201	0.761 ± 0.0657	−12.3
GreyPro	2.6	2.36 ± 0.15	1.79 ± 0.11	−24.3
Rigid10k	11	12.0 ± 1.14	9.30 ± 0.60	−22.4
Titanium	113.8	119. ± 2.55	119. ± 8.19	0.56
Inconel	200	198. ± 5.32	185. ± 16.7	−6.2

Table 5
Dogbone ultimate tensile strength.

	Published [MPa]	Dry [MPa] ± SD	Wet [MPa] ± SD	Change [%]
Essentium	74.5	60.8 ± 0.959	29.4 ± 0.347	−51.6
Onyx	37	35.9 ± 0.268	24.8 ± 0.101	−31.0
GreyPro	61	54.7 ± 0.531	35.6 ± 1.57	−34.8
Rigid10k	81	57.4 ± 2.44	46.0 ± 3.43	−19.8
Titanium	993	969 ± 0.806	961 ± 11.6	−0.8
Inconel	993	1078 ± 1.48	1094 ± 12.6	1.5

Table 6
Dogbone maximum strain.

	Dry [%] ± SD	Wet [%] ± SD	Change [%]
Essentium	3.44 ± 0.127	8.78 ± 0.978	154
Onyx	64.6 ± 19.4	38.8 ± 3.84	−39.9
GreyPro	9.26 ± 3.00	8.24 ± 1.30	−11.0
Rigid10k	0.675 ± 0.017	0.792 ± 0.110	17.3
Titanium	13.4 ± 0.516	16.6 ± 0.698	24.0
Inconel	31.2 ± 1.09	30.2 ± 1.44	−3.2

2.5. Profilometry measurements

Surface finish for the two-bladed rotors was measured using a Keyence VR-5000 optical profilometer to quantify the material roughness as retrieved from the printer. Measurements were scanned using a high (40x) magnification, where a small portion of the outer surface of each blade was scanned to cover an area including the leading and trailing edges. Using the profilometer's native software, the image's background was removed to eliminate background surfaces, and the tilt of the blade within the imaging frame was removed using the instrument's reference plane tool. The 2D surface of the blade was flattened to a 1D surface using the software's waveform tool. Resulting scans were then trimmed to eliminate edge effects post-correction before computing surface statistics.

The surface finish statistics measured were arithmetical mean height, root-mean-square (RMS) height, skewness, and kurtosis. Mean height expresses, as an absolute value, the height of each surface feature relative to the arithmetical mean of the surface. RMS height is equivalent to the standard deviation of surface features from the arithmetic mean. Skewness represents the degree of bias towards roughness peaks or valleys, and kurtosis is a measure of the tailedness of the roughness distribution. These measurements offer a qualitative indication of how much post-processing a print may require.

2.6. 3D scan measurements

Three dimensional digital models were created for each of the two-bladed rotors using a handheld EinScan Hx scanner to measure structural warping. To facilitate scanning, a 3D scanning spray was applied to haze the rotors. Reflective stickers were applied to each rotor to provide fixed reference points for the scanner. Two scans of each rotor were taken and merged, any holes were filled and rough surfaces were smoothed with the EX Scan software. Lastly, the scans were aligned to the principle axis using MeshLab software and refined manually.

3. Results

3.1. Tensile tests and environmental conditioning

The environmental conditioning tests showed that while no degradation in the metal materials was observed, significant degradation occurred in the carbon-fiber-based samples, mild degradation occurred in the pure thermoplastics, and little to no degradation was observed in the metal samples. Material degradation was quantified by examining the stress–strain curves and measuring the elastic moduli and ultimate tensile strength (UTS). The stress–strain curves for all material samples are shown in Fig. 5, and the weight change, elastic moduli, and ultimate tensile strength are shown in Tables 3–6.

The carbon-based materials' properties changed drastically, losing significant rigidity and strength after environmental conditioning. The average elastic moduli dropped 63.8% and 12.3% for Essentium and Onyx, respectively, while the average ultimate tensile strength weakened by 51.6% and 31.0% respectively. Maximum strain increased by 154% for the Essentium samples and decreased by 39.9% for the Onyx dogbones. Because of significant degradation after environmental conditioning, the carbon-reinforced nylon materials were not considered for turbine manufacturing.

The Formlabs resin thermoplastics also lost strength after environmental conditioning. GreyPro had similar losses to the Onyx samples in terms of percent change, while Rigid10k better retained strength (Table 5). The dry GreyPro samples had an average elastic modulus of 2.36 GPa and ultimate tensile strength of 54.7 MPa, compared to a published modulus of 2.6 GPa and UTS of 61 MPa (Formlabs, 2024a). After seawater immersion, the average elastic modulus was reduced to 1.79 MPa, a 24.3% reduction, while UTS is similarly reduced by 34.8% to an average of 34.8 MPa (see Table 6).

The print quality of the Formlabs Rigid10k was much more varied than the GreyPro material among the dry samples. Rigid10k material properties are nearer to a ceramic than a plastic polymer, and they have no obvious yield point on the stress–strain curve (Fig. 5e). The elastic moduli is more difficult to measure on these samples because they quickly undergo inelastic deformation with strain. The published elastic modulus and UTS for Rigid10k are 11 GPa and 81 MPa (Formlabs, 2024b), respectively, and the mean dry sample measured properties were 12.0 GPa and 57.4 MPa, respectively. The environmentally conditioned Rigid10k samples had an average elastic modulus of 9.30 GPa and UTS ranging from 46.0 MPa, a reduction from the dry samples of 22.4% and 19.8%, respectively.

Environmental conditioning of the metal samples did not produce significant material property changes. The average elastic moduli decreased less than 1% on the titanium parts and, though it dropped 6.2% on the Inconel parts. Little change was observed in UTS in the titanium and Inconel stress–strain curves, with a reduction in UTS of less than 1% and an increase in UTS of 1.5%, respectively. The dry metal sample material properties were fairly similar, though not equal, to the published properties. The published elastic moduli and UTS for DLMS-printed titanium are 113.8 GPa and 993 MPa (Protolabs, 2026b), while the mean printed properties were 119 GPa and 969 MPa, respectively. The published and printed elastic moduli of DLMS-printed Inconel are 200 and 298 GPa, respectively, and 993 and 1078 MPa for UTS, respectively (Protolabs, 2026a). After environmental conditioning, the maximum strain of the titanium samples increased by 25%, suggesting raw seawater exposure caused the printed alloy to become more ductile.

3.2. Surface finish measurements

Profilometer measurements characterized the surface roughness, or change in surface height across the measurement area, in terms of the mean, standard deviation, skew and kurtosis, following the ISO 21920-

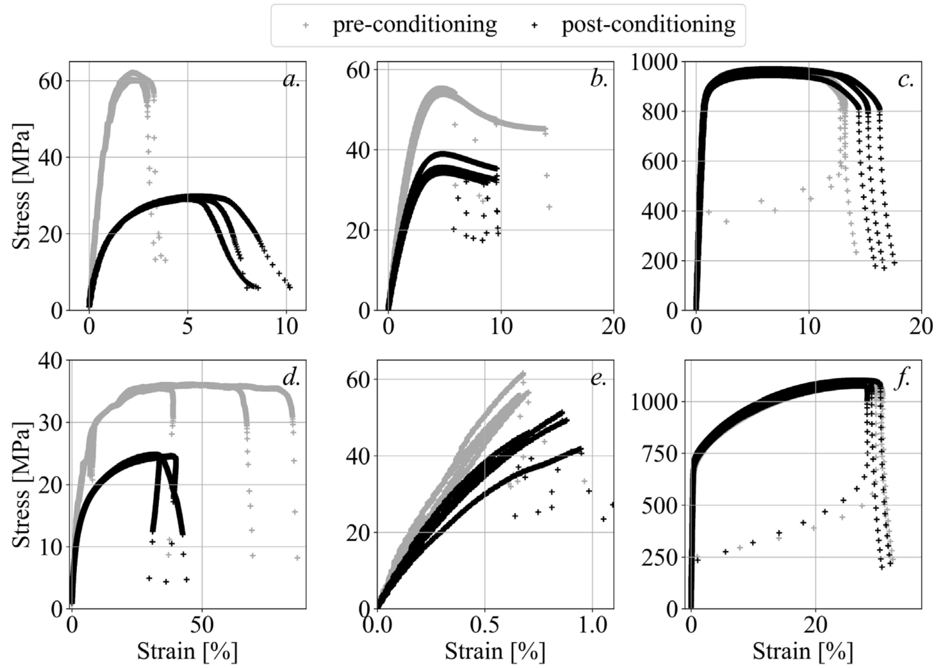

Fig. 5. Stress–strain curves for dry and environmentally conditioned material samples: Essentium HTN-CF25 (a.), Formlabs GreyPro (b.), Titanium Ti–6Al–4V (c.), Markforged Onyx (d.), Formlabs Rigid10k (e.), and Inconel 718 (f.). Note axes limits are not consistent between subplots.

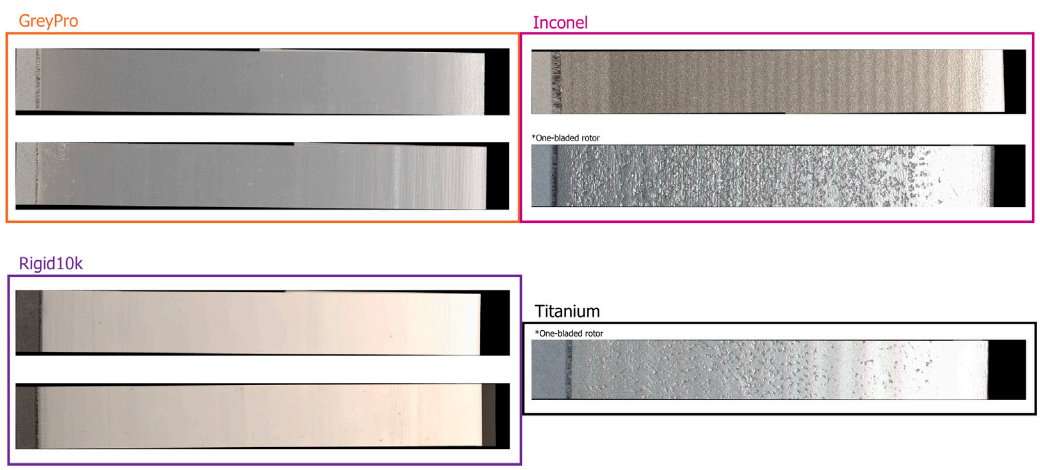

Fig. 6. Profilometer images for the one and two-bladed rotors.

Table 7
Surface Roughness statistics for two-bladed rotors and metal one-bladed rotors.

	GP-sharp	GP-lofted	R10k-sharp	R10k-lofted	In-sharp	In-sharp[a]	Ti-sharp[a]
Mean [μm]	10.285	12.716	6.246	13.238	11.348	26.459	7.944
RMS [μm]	20.027	24.794	10.049	24.016	18.710	39.036	15.305
Skew	5.052	5.019	2.894	4.160	3.172	−1.552	−2.035
Kurtosis	39.171	37.858	14.284	24.884	16.414	7.389	19.789
Measured Area [cm^2]	12.80	12.99	14.08	13.38	13.62	13.63	13.04

[a] one-bladed rotor.

2 standard (ISO 21920-2:2021, 2021). Images from the profilometer for the rotors are shown in Fig. 6. The Formlabs rotors did not require post-processing and surface measurements were representative of the surface quality directly post-print. The metal rotors required finishing to remove support material from the raw prints. From the results shown in Table 7, all of the two-bladed rotors had similar roughness statistics, with mean surface feature heights on the order of 10 μm and standard deviations at around twice the mean. The one-bladed metal rotors had a different surface finish compared to the two-bladed Inconel rotor, with more noticeable pitting, quantified by negative skew.

Skew provides information on the spread, height and distribution of surface roughness. The skew of the roughness feature distributions is greater than zero and less than 6 for the two-bladed rotors, and less than zero for the one-bladed metal rotors. Skewness below zero means that the surface height is primarily above the mean roughness plane (e.g., there are deep pits or rifts in the surface); above zero means the

Table 8
L2 norms for each blade centerline [z/L].

	Blade 1	Blade 2
GP lofted	1.4	1.3
GP sharp	1.4	2.3
R10k lofted	0.71	0.81
R10k sharp	1.1	0.67
In sharp	2.0	3.1
Ti sharp	0.92	–

surface height is primarily below the mean roughness plane (e.g., there are tall ridges or peaks in the surface).

Kurtosis describes the outliers in a distribution; for surface roughness this equates to the variety of peaks and valleys far above or below the mean roughness plane (kurtosis greater than 3) or lack thereof (less than 3). A kurtosis of 3 suggests the surface roughness features are normally distributed about the mean surface plane. With values well above 3, all of these printed rotors then contain a wide ranging variety of surface features, with the GreyPro rotors having the most extreme feature variation. It is possible that the surface finishing on the metal rotors helped reduced this statistic.

While the roughness statistics in Table 7 help quantify differences in surface finish between the rotors, the profilometry images in Fig. 6 show a more variable surface quality for the metal printed rotors than the thermoplastic rotors. This is most apparent in the one-bladed metal rotors where the manufacturing process resulted in clear pitting. Qualitatively, and evidenced by negative skew, the pitting is worst for the one-bladed metal rotors. The two-bladed Inconel rotor lacked this pitting and qualitatively had the most consistent surface finish of the metal rotors.

3.3. 3D scan results

Deformation (warping) of the printed two-bladed turbine rotors relative to the nominal design was observed in the 3D scan results (Fig. 7). The GreyPro lofted-joint turbine (a) had two large chips in the 3D scans that were not present during the performance testing. The turbine blades were subject to warping in the radial and tangential directions. In other words, the blades warped to and away from the center shaft as seen in the front and back views, and curvature of the leading and trailing edges is clear in the side views (most evident for the sharp joint GreyPro rotor, Fig. 7b).

The warping in the blade length and chord plane was quantified by computing the centerline of each blade from the 3D scan meshes using an open-source software called Blender. To do this, the mesh files were imported into Blender and scaled to nondimensionalize the rotor based on its blade length. Each rotor was then divided in half along the shaft axis and saved as individual files (one blade mesh per file). Then, on each blade, 16 evenly-spaced cross-sections were sliced along the blade between the blade–strut joints. The volume-weighted center-point of each cross-section slice was then found, forming an along-blade centerline composed of 16 datapoints. Each datapoint in the centerline represents the distance between it and the mean in the along-chord direction. Note, each slice must be a volume rather than an area because the mesh itself is made from thousands of vertices that are not perfectly aligned on any particular plane. The L2 norm for each blade centerline is shown in Table 8, where an L2 norm of 0 represents a perfectly straight centerline. A best fit line in the form of a 3rd-order polynomial was fit to each centerline and is shown in Fig. 8.

The most substantial warping of the turbine blades occurred for the GreyPro sharp-joint turbine (b) and the Inconel rotor (e) (Figs. 7 and 8). These rotors have the largest differences between the L2 norm of each blade (Table 8). The Rigid10k rotors consistently have the least amount of warping (visually and as quantified by the L2 norm), as does the 1-bladed titanium rotor. The Formlabs rotors were observed to warp during the required curing process post-print, after the support structures are removed. It is possible the Rigid10k's stiffness reduced the post-process warping versus the more compliant GreyPro. The Inconel rotor has a deformation from the nominal straight-blade design near the bottom strut, indicative of a "shift line" defect in the print (see Appendix), which results in it having the largest L2 norm.

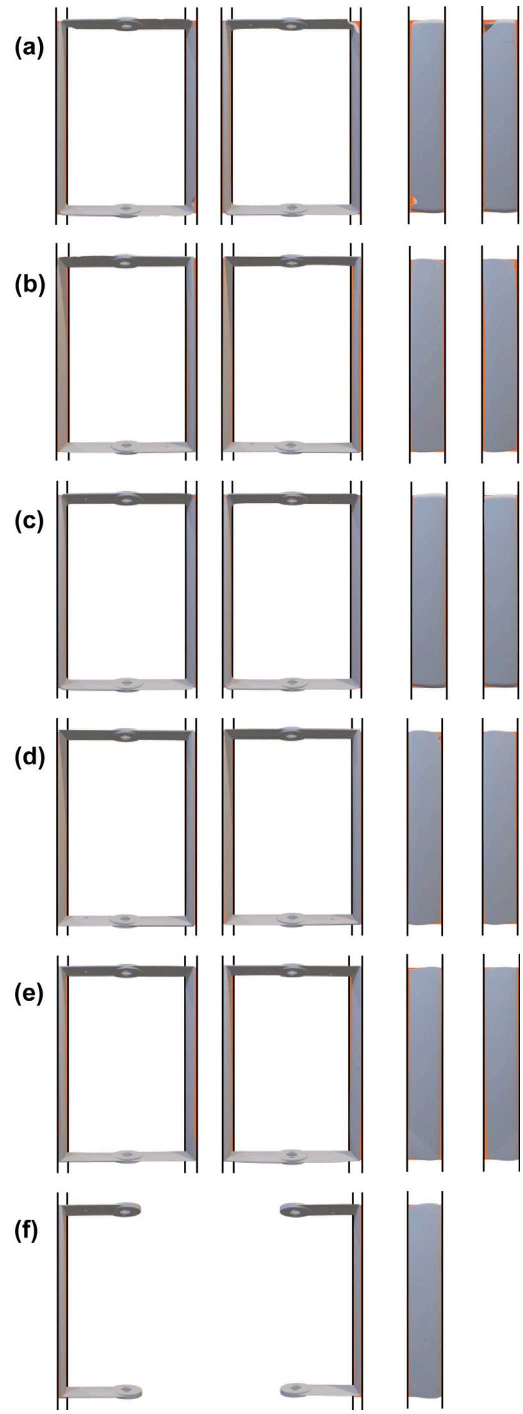

Fig. 7. Front, back and side views of printed rotors. (a) GreyPro lofted-joint turbine. (b) GreyPro sharp-joint turbine. (c) Rigid10k lofted-joint turbine. (d) Rigid10k sharp-joint turbine. (e) Inconel sharp-joint turbine (f) Titanium single-bladed turbine. Deviance from the black vertical lines, highlighted in orange, signifies blade warping.

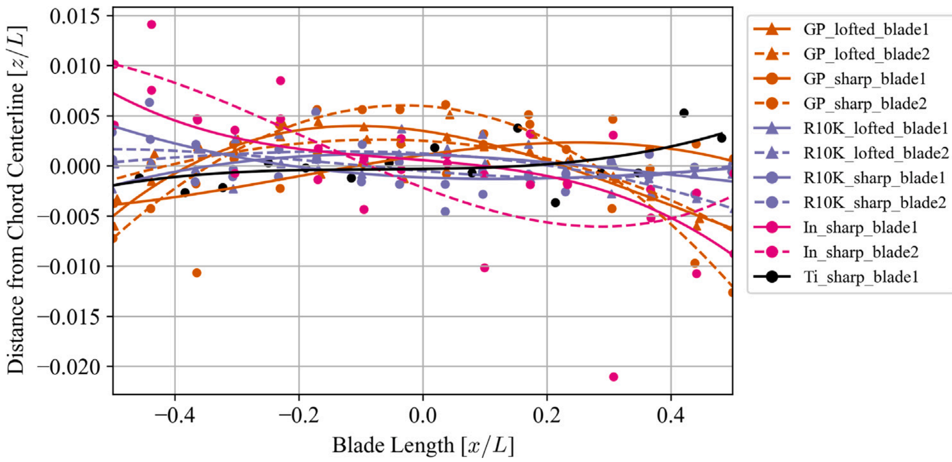

Fig. 8. Rotor blade centerlines normalized by blade length (L): distance along blade (x) versus distance from mean chord (z). Curves show the best-fit 3rd-order polynomial to improve visual comparison. Blade 1 is the upstream blade when phase angle is at 0 degrees.

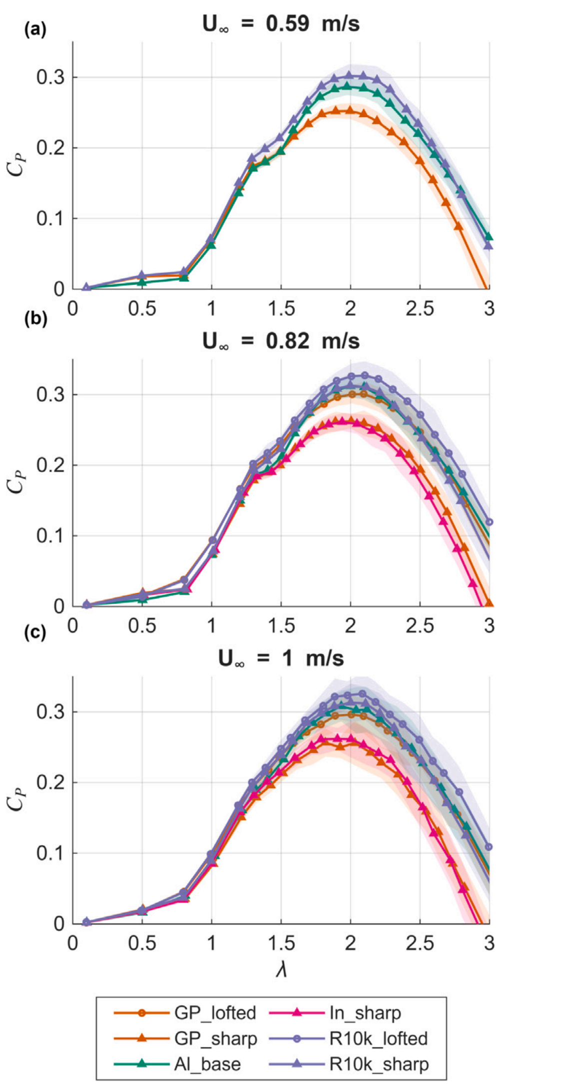

Fig. 9. Time-averaged performance results for the two-bladed GreyPro (GP), Rigid10k (R10k), Inconel (In), and Aluminum (Al) rotors at three inflow velocities. Shaded region is the standard deviation of individual cycle-averages.

3.4. Flume results

Time-averaged performance curves for the two-bladed rotors are shown in Fig. 9. Both Rigid10k rotors matched or outperformed the aluminum rotors at the performance peak for all three inflow velocities, and the lofted joint Rigid10k rotor had the highest peak performance of all two-bladed rotors ($C_P = 0.32$ at $U_\infty = 1$ m/s). The Inconel and GreyPro sharp-joint rotors performed the worst, having peak performances at $U_\infty = 1$ m/s of $C_P = 0.26$ and $C_P = 0.27$, respectively. The lofted joint rotors outperformed the sharp joint rotors, especially at higher tip–speed ratios, which is consistent with prior simulation work (Villeneuve et al., 2021). Performance differences between joint types were greater between the GreyPro rotors than between the Rigid10k rotors, likely because the differences in geometric shape between the GreyPro rotors due to warping was greater than for the Rigid10k rotors (Table 8). In particular, the two-bladed sharp-joint GreyPro rotor has substantial warping on both blades which might explain its poor performance relative to the other thermoplastic prints (Fig. 7).

The aluminum and thermoplastic rotors were tested at three freestream velocities to assess if the reduced structural rigidity of the thermoplastic rotors impacted turbine performance. Time-average performance curves are presented in Fig. 10 for the aluminum rotor compared to the sharp joint GreyPro and Rigid10k rotors. Peak time-averaged performance increased slightly between $U_\infty = 0.59$ and 0.82 m/s for all rotors. Peak performance is consistent between $U_\infty = 0.82$ and 1 m/s for the Rigid10k rotors, but peak performance for the aluminum and GreyPro rotors is slightly lower for $U_\infty = 1$ m/s than for $U_\infty = 0.82$ m/s. Overall, the performance differences with U_∞ are larger for the aluminum rotor than for the thermoplastic rotors. Therefore, at this scale, these results do not clearly point to significant performance losses due to deformation of the thermoplastic rotors under increased thrust.

Turbine performance throughout a rotation (phase-averaged performance) for the two-bladed rotors is presented for $\lambda = 2.5$ in Fig. 11. If the blades in a turbine were identical, symmetry would be expected between the two phase-averaged performance peaks. This is true for the baseline aluminum rotor, but asymmetry between performance peaks is evident for the printed rotors. The difference between maximum performance for the two performance peaks, ΔCP_{peak}, is shown in Fig. 11b, and is most pronounced for the GreyPro and Inconel rotors. This result is in line with the 3D scan results which show the most substantial warping for these rotors (Figs. 7 and 8 and Table 8).

The one-bladed rotors were tested to provide further insight into the observed performance differences. Time-averaged performance curves for the one-bladed rotors are shown in Fig. 12. Inconsistencies are apparent between the one- and two-bladed results. For example, the

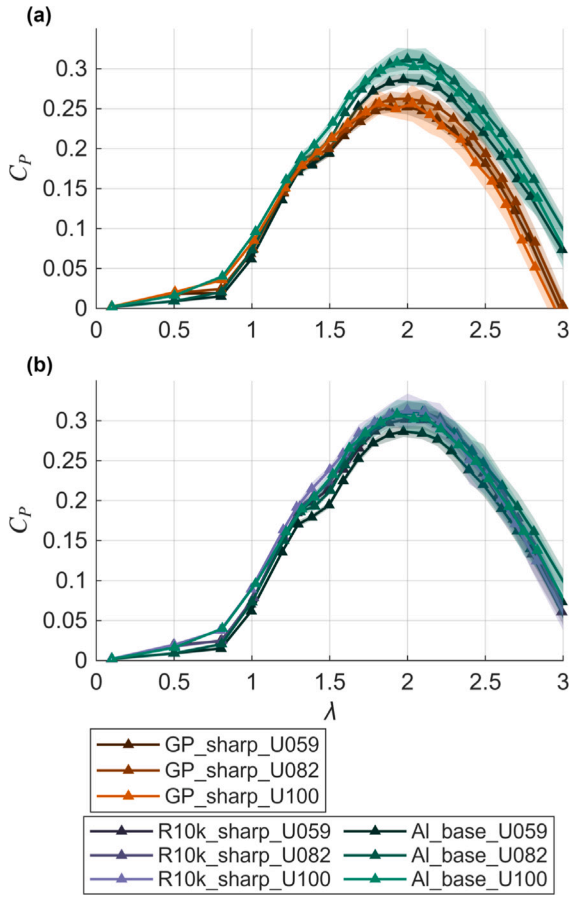

Fig. 10. Time-averaged performance as a function of inflow speed for the (a) GreyPro (GP), (b) Rigid10k (R10k) sharp-joint rotors compared to the aluminum (Al) rotor. 'U059' denotes U_∞ = 0.82 m/s, 'U082' denotes U_∞ = 0.59 m/s and 'U100' denotes U_∞ = 1 m/s. Shaded region is the standard deviation of individual cycle-averages.

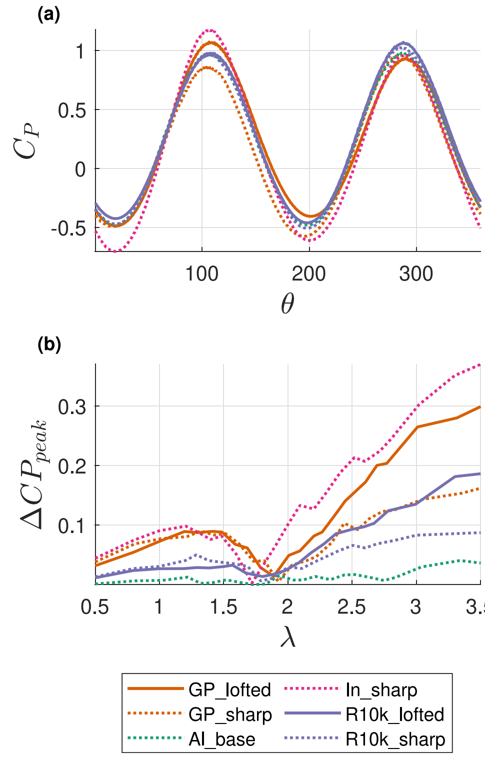

Fig. 11. Phase-averaged performance for the two-bladed GreyPro (GP), Rigid10k (R10k), Inconel (In), and Aluminum (Al) rotors at U_∞ = 1 m/s and λ = 2.5.

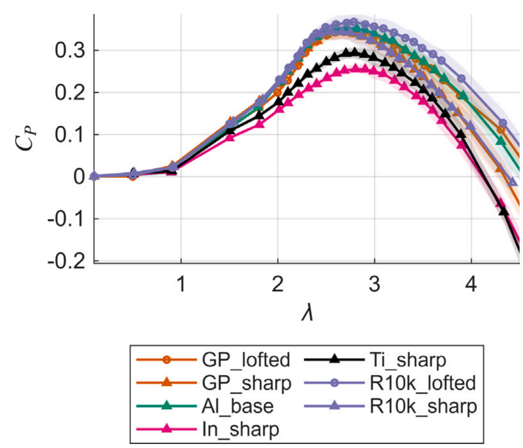

Fig. 12. Time-averaged performance results for the one-bladed GreyPro (GP), Rigid10k (R10k), Inconel (In), Titanium (TI) and Aluminum (Al) rotors. U_∞ = 0.82 m/s. Shaded region is the standard deviation of individual cycle-averages.

two-bladed sharp-joint Inconel and GreyPro rotors have similar performance, but the one-bladed GreyPro sharp-joint rotor far outperforms the equivalent Inconel rotor. Additionally, the difference in peak performance between the lofted- and sharp-joint rotors is larger for the GreyPro rotors in the two-bladed prints than for the one-bladed prints. Comparatively, performance differences between joint types are consistent for the one- and two-bladed Rigid10k rotors. The variable GreyPro results are likely related to the substantial blade-to-blade asymmetry in the two-bladed GreyPro rotors (Fig. 11). Despite these inconsistencies, several results are common between the one- and two-bladed results in Figs. 9 and 12: (1) the lofted-joint consistently improved performance over the sharp-joint rotors, (2) the Rigid10k lofted-joint rotor consistently outperformed all other rotors, and (3) the metal prints consistently performed the worst.

Normal and tangential force coefficients for each of the one-bladed rotors were investigated to elucidate the drivers of performance differences between prints. Fig. 13 shows the normal and tangential force coefficients averaged over the upstream (0° – 180°) and downstream (180°–360°) sweeps for the one-bladed rotors. Compared to the range of force coefficients across the tested tip–speed ratios, the material/joint type had a more limited impact on the normal force than on the tangential force (a–d). However, when baseline subtracted (e–h), differences between material/joint type were comparable in the normal and tangential force coefficients. Some notable observations include:

1. The tangential force coefficients for the metal prints are lower than for the other prints in the upstream and downstream sweeps. Specifically, the titanium and Inconel rotors have negative tangential force coefficients for all tip–speed ratios in the downstream sweep. These results are consistent with the metal-printed rotors experiencing more drag than the thermoplastic prints and could be related to poor surface quality (Fig. 6) and/or print geometry. The Inconel rotor had the most negative tangential force coefficients, the largest mean surface feature height (0.007c) and standard deviation Table 7, and also visually the worst variable surface finish of the rotors (Fig. 6. This finding is inline with (Stringer and Polagye, 2020) who show a reduction in cross-flow turbine performance with an increase in barnacle roughness element size, even for barnacles as small as 0.007c.

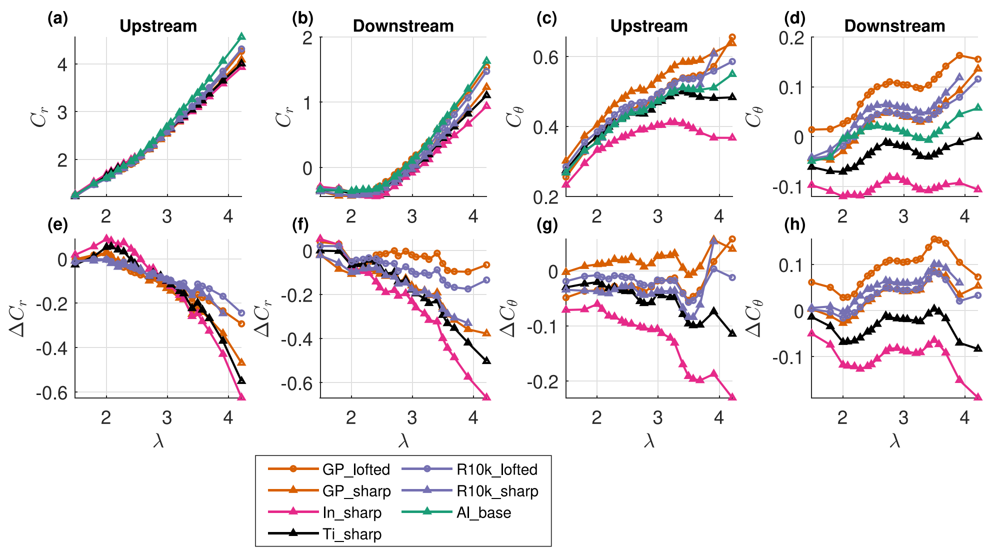

Fig. 13. Blade-level forces for the one-bladed GreyPro (GP), Rigid10k (R10k), Inconel (In), Titanium (TI) and Aluminum (Al) rotors. (a–d) Upstream (0° – 180°) and downstream (180° – 360°) averaged normal and tangential force coefficients for U_∞ = 0.82 m/s. (e–h) Baseline subtracted, relative to the baseline aluminum rotor, upstream and downstream averaged normal and tangential force coefficients.

2. The baseline subtracted results reveal higher normal force coefficients for the lofted-joint rotors than the sharp-joint rotors in the downstream sweep. This is most evident at high tip–speed ratios. As the tip–speed ratio increases, the direction of lift becomes increasingly normal to the blade path (particularly in the downstream sweep) (Snortland et al., 2025a). Therefore, the higher normal force coefficients are indicative of lofted-joints improving lift generation and/or reducing induced drag as found by Villeneuve et al. (2021).

In sum, the metal printed rotors likely performed worse than the other rotors in part because of higher drag from poorer print or surface quality, and lofted-joint rotors might have outperformed sharp-joint rotors because of increased lift.

4. Discussion

4.1. Materials selection

Investigating how material properties degrade in seawater is critical for any ocean engineering application. While composites like fiberglass are commonly used in the marine space (Mouritz et al., 2001), carbon composites degrade in seawater because the water causes the fiber to debond and delaminate from the resin matrix (Siriruk and Penumadu, 2014; Koshima et al., 2019). This same phenomenon is likely responsible for the degradation of the carbon-based AM materials in the form of reduced elastic moduli and ultimate tensile strength (Fig. 2), even though they do not contain continuous fibers. Mild degradation of the Formlabs resin materials occurred, consistent with most thermoplastics that have been tested, except for a select few, such as Ultem 9085 (Murdy et al., 2023). Thermoplastic materials showed usefulness for swift prototyping and testing of multiple geometries while requiring little to no manual post-processing. Unsurprisingly, titanium and Inconel were largely unaffected by submersion in seawater and retained their strength characteristics. Unfortunately, the metal prints were the most difficult to fabricate (see Appendix) and resulted in the poorest print quality (see Figs. 6 and 7). Because of these reasons, future work on AM cross-flow rotor design would benefit from the ability to rapidly prototype using thermoplastics, but incorporate metal AM materials near the end of the design phase and before creation of a final prototype.

4.2. Rotor printing and flume testing

Cross-flow turbine performance curves were sensitive to print quality, namely surface finish and part warping caused by uneven heat dissipation or curing effects. Even minor warping (Figs. 7 and 8, Table 8) caused noticeable decreases in power performance (Fig. 9) and asymmetry in rotor performance (Fig. 11). The highest quality prints, the Rigid10k rotors, performed on par with the aluminum rotor used as an experimental control.

To mitigate the warping issue in the future, the one-bladed rotor design could be updated to allow multiple one-bladed prints to attach to a single shaft. This would minimize warping associated with the two-bladed prints and allow multiple-blade rotors (3+) to be constructed. The benefit of this method is that three- and four-bladed rotors, while less efficient than two-bladed versions, have lower torque and force fluctuations, reducing fatigue on the generator and turbine structure (Hunt et al., 2024). How the fabrication process affects the structural integrity and fatigue life of the rotor, however, is a subject for future work.

If the warping issue can be resolved, one benefit of additive manufacturing for producing turbine rotors is the ability to rapidly test new, unique geometries that would otherwise be cost prohibitive to manufacture. For example, the lofted blade–strut joint would be expensive to manufacture with traditional methods, but the two-bladed lofted-joint Rigid10k rotors were each printed and cured in ~9 h and required minimal human-hour input beyond design time. In this way, AM methodologies show promise in facilitating rapid, economic, and comprehensive research studies on cross-flow turbine design.

Surface roughness is attributed to the performance degradation (Stringer and Polagye, 2020) and had a larger affect on the metal rotors, in particular on those with a pitted surface finish. The 1-bladed titanium rotor, for instance, was one of the least warped of the rotors (Table 8), yet still did not have a comparable performance to the aluminum control rotor. At larger scales, the impact of surface roughness (i.e., drag losses) should decrease. Assuming the AM-print process is consistent, the surface quality would be expected to remain the same, but the size of individual roughness elements relative to the blade chord-length would decrease. In this respect, printed rotors will become relatively smoother at larger scales.

4.3. Blade deflection

In terms of deflection, if we assume the rotor blades are simply supported beams, we can quickly estimate the maximum blade deflection δ seen during flume experiments using $\delta = (FL^3)/(48EI)$. With $Cr = 4$ from Fig. 13, the blade length L, an area moment of inertia $I = 0.624x10^{-9}\text{m}^4$ (computed using XFOIL Drela, 1989 for the NACA0018 blade geometry), and the dry sample elastic moduli E from Table 4, we can compute the maximum deflection for the GreyPro rotors to be on the order of 10 mm. For GreyPro, this is a similar order of magnitude as the blade warpage, and could explain why the GreyPro lofted rotor's peak performance is slightly lower than the control rotor's (Fig. 9). This does not, however, explain the noted drop in performance between the 0.82 m/s and 1 m/s test cases, where the aluminum control rotor also saw a performance decrease. This deflection estimation scales with $1/E$, which, for the other materials, would then have had less than 2 mm of deflection in the flume.

Contrarily to surface finish, as rotors are scaled up for the field, they become relatively less stiff. For a constant geometry (i.e. chord-to-radius ratio and turbine aspect ratio), material and print orientation, the bending stiffness of the blades, EI, will scale as D^4, the fluid and centripetal forces will scale with $D^2U_\infty^2$ and the blade span will scale with D. Blade deformation, $\delta \propto FS^3/EI$, scales as DU_∞^2, so for a given freestream velocity, δ will increase with scale but the ratio δ/D (i.e. the deformation as a fraction of the turbine diameter) is constant. However, viable tidal sites typically have freestream current speeds greater than 1 m/s (the highest inflow tested here) and δ/D scales as U_∞^2. Evidence of significant deformation was not obvious in these experiments but could be at scale. Further, because of an-isotropy of many 3D printed materials, changes to print orientation by manufactures or as required by print bed constraints could impact the bending stiffness and blade deformation.

5. Conclusions

To be suitable for the marine environment and use in the marine renewable energy industry, fabrication methods incorporating AM materials should be as robust and perform as well or better than rotors made with conventional manufacturing methods. This study investigated the suitability of AM to fabricate cross-flow turbine rotors by looking at possible AM materials and comparing material and performance results to a turbine with blades made with conventional manufactured techniques at a small scale. Some of the thermoplastic rotors had inconsistent performance due to rotor warping from the curing process, while the metal rotors consistently performed worse than the others because of poorer print quality in terms of warping, surface finish, and the 2-bladed rotor's blunted trailing edge. A lofted blade–strut joint consistently improved performance over a sharp joint, which is likely related to increased lift production. At this scale, the estimated blade deformation during flume testing was on the same order of magnitude for the more compliant thermoplastic rotors, and so may have decreased their performance but it did not significantly affect the other, stronger materials.

While it is unlikely that current AM technology can be used to fabricate an entire rotor at a larger scale, the results from the small-scale show that there could be promise in incorporating AM techniques into the fabrication of a large-scale design as well as using it to fabricate difficult-to-manufacture geometries. AM could create designs that mitigate stress concentrations by creating lofted geometries and removing sharp edges, though further investigation into the structural resilience of such a rotor is needed. Future work should include rotor testing of structural properties and fatigue life, which were not completed here, as well as how to improve the quality of metal printing. These aspects will be critical to the success of larger-scale rotors if they are to be deployed in the field.

CRediT authorship contribution statement

James R. McVey: Writing – original draft, Visualization, Supervision, Methodology, Formal analysis, Data curation, Conceptualization. **Abigale C. Snortland:** Writing – original draft, Visualization, Formal analysis, Data curation. **Christopher R. Rumple:** Writing – review & editing, Investigation, Formal analysis. **John T. Zaengle:** Resources, Methodology, Investigation. **Robert J. Cavagnaro:** Writing – review & editing, Supervision, Project administration, Funding acquisition, Conceptualization. **Michelle D. Fenn:** Resources, Project administration. **Gregory Talpey:** Methodology, Investigation. **Emma N. Geon:** Investigation.

Declaration of competing interest

The authors declare that they have no known competing financial interests or personal relationships that could have appeared to influence the work reported in this paper.

Acknowledgments

The authors would like to thank Tim Roosendaal and Rob Seffens for conducting mechanical load testing of material samples for the environmental conditioning tests, Brittnee Lommers for printing the thermoplastic dogbone samples, Daniel Merkel for taking profilometry measurements, and Riley Cannon for creating the 3D scans of the rotors.

This work was authored by the Pacific Northwest National Laboratory, operated by Battelle Memorial Institute for the U.S. Department of Energy (DOE) under Contract No. DE-AC05-76RL01830. This study is funded by the U.S. Department of Energy Office of Critical Minerals and Energy Innovation, Water Power Technologies Office. The views expressed herein do not necessarily represent the views of the DOE or the U.S. Government.

Appendix. Metal DMLS printing

Printing in metal proved to be a nontrivial aspect of this work, primarily for 3 main issues during the printing process: melting, warping, and shift lines. All three of these problems were dependent on the DMLS process and structure of the part, though warping is a common problem when printing with thermoplastics. The final rotor design specifications were a result of designing a rotor that could be printed in metal and reduce these issues.

Melting and warping were caused by inconsistent heat transfer — a design with major changes in cross-sectional area appeared more at risk for melting and warping because different regions of the part cool at different rates, inducing thermal stresses. Fig. A.14a. show images of an early design, where trailing edges melted and the blades warped. The other difficult problem was shift lines, a phenomena where the sintered material on a narrow cross-section shifts a fractional amount because of insufficient support provided to it. This was a function of trailing edge thickness and the fraction of printing volume taken up by the part. It was a problem around sharp corners and was a fundamental issue with the two-bladed part design (Fig. A.14b). To avoid this issue, the trailing edge was blunted to provide a wider surface for the support structure to bond to.

The one-bladed design required less print volume space, which allowed for more robust support structures and did not have the shift line problem. One of the successful single-bladed metal rotors is shown in Fig. A.14c. Because of the greater success printing one-bladed rotors in metal, future work involving larger or multi-bladed rotors should focus on printing single blades that are designed to mount on a central shaft. Finally, surface finish could vary between the metal parts, depending on the post-processing required to remove support structure material.

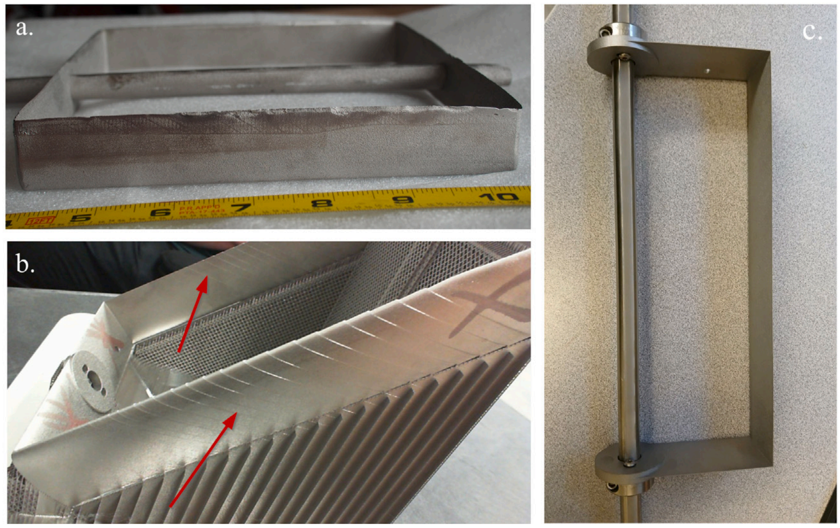

Fig. A.14. Examples of test metal prints: (a.) melting and warping, (b.) shift lines on a prototype part, (c.) successful one-bladed print.

References

ASTM International, 2021. ASTM E8 / E8M, Standard Test Methods for Tension Testing of Metallic Materials. Technical Report, ASTM International, West Conshohocken, PA, URL https://www.astm.org/Standards/E8.

Bassett, C., Gibbs, P., Wood, H., Cavagnaro, R.J., Cunningham, B., Dosher, J., Joslin, J., Polagye, B., 2025. Lessons learned from the design and operation of a small-scale cross-flow tidal turbine. J. Ocean. Eng. Mar. Energy 1–21. http://dx.doi.org/10.1007/s40722-025-00411-y.

Bichanich, M., Bharath, A., O'Byrne, P., Monahan, M., Ross, H., Raye, R., Nichols, C., Candon, C., Wosnik, M., 2025. In-situ blade strain measurements and fatigue analysis of a cross-flow turbine operating in a tidal flow. Renew. Energy 239, 121977. http://dx.doi.org/10.1016/j.renene.2024.121977.

Chaudhary, B., Li, H., Matos, H., 2023. Long-term mechanical performance of 3D printed thermoplastics in seawater environments. Results Mater. 17, 100381. http://dx.doi.org/10.1016/j.rinma.2023.100381.

Dong, S., Zhou, P., Ning, Z., Wu, X., Li, C., Xian, G., 2024. Durability of carbon- and glass-fiber reinforced thermoplastic polymer composites: A literature review. J. Build. Eng. 111055. http://dx.doi.org/10.1016/j.jobe.2024.111055.

Drela, M., 1989. XFOIL: An analysis and design system for low Reynolds number airfoils. In: Low Reynolds Number Aerodynamics: Proceedings of the Conference Notre Dame, Indiana, USA, 5–7 June 1989. Springer, pp. 1–12.

Essentium, 2020. Essentium HTN-CF25 technical datasheet, Rev. 1.0 ed. URL https://nexa3d.com/wp-content/uploads/2024/07/TDS-Essentium-HTN-CF25.pdf.

Formlabs, 2024a. Grey pro resin technical datasheet, Rev. 01 ed. URL https://formlabs.com/store/materials/grey-pro-resin/. Document Number: 1801086.

Formlabs, 2024b. Rigid 10k resin technical datasheet, Rev. 06 ed. URL https://formlabs.com/store/materials/rigid-10k-resin/. Document Number: 2001479.

Ghabezi, P., Flanagan, T., Walls, M., Harrison, N.M., 2025. Degradation characteristics of 3D printed continuous fibre-reinforced PA6/chopped fibre composites in simulated saltwater. Prog. Addit. Manuf. 10 (1), 725–738. http://dx.doi.org/10.1007/s40964-024-00654-5.

Gonabadi, H., Hosseini, S.F., Chen, Y., Bull, S., 2024. Structural analysis of small-scale 3D printed composite tidal turbine blades. Ocean Eng. 306, 118057. http://dx.doi.org/10.1016/j.oceaneng.2024.118057.

González-Montijo, M., Murdy, P., Candon, C., Beach, R., Nichols, C., Barden, P., 2023. Additive Manufacturing for Powering the Blue Economy Applications: A Tidal Turbine Blade Case Study. Technical Report, National Renewable Energy Laboratory, Golden, CO (United States), http://dx.doi.org/10.36688/ewtec-2023-420.

Harrold, M., Ouro, P., 2019. Rotor loading characteristics of a full-scale tidal turbine. Energies 12 (6), 1035. http://dx.doi.org/10.3390/en12061035.

Howell, R., Qin, N., Edwards, J., Durrani, N., 2010. Wind tunnel and numerical study of a small vertical axis wind turbine. Renew. Energy 35 (2), 412–422. http://dx.doi.org/10.1016/j.renene.2009.07.025.

Hunt, A., Strom, B., Talpey, G., Ross, H., Scherl, I., Brunton, S., Wosnik, M., Polagye, B., 2024. An experimental evaluation of the interplay between geometry and scale on cross-flow turbine performance. Renew. Sustain. Energy Rev. 206, 114848. http://dx.doi.org/10.1016/j.rser.2024.114848.

International Organization for Standardization, 2019. Plastics — Determination of tensile properties — Part 1: General principles. URL https://www.iso.org/standard/527-1.

ISO 21920-2:2021, 2021. Geometrical Product Specifications (GPS) — Surface texture: Profile — Part 2: Terms, Definitions and Surface Texture Parameters. International Organization for Standardization, Geneva, Switzerland, Standard. URL https://www.iso.org/standard/72226.html.

Koshima, S., Yoneda, S., Kajii, N., Hosoi, A., Kawada, H., 2019. Evaluation of strength degradation behavior and fatigue life prediction of plain-woven carbon-fiber-reinforced plastic laminates immersed in seawater. Compos. Part A: Appl. Sci. Manuf. 127, 105645. http://dx.doi.org/10.1016/j.compositesa.2019.105645.

LeBlanc, J., Shattuck, L., Warner, E., Javier, C., Chenwi, I., Torres, J., Ponte, D., Lockhart, P., Chu, T., Shukla, A., 2024. High pressure salt water and low temperature effects on the material performance characteristics of additive manufacturing polymers. Int. J. Light. Mater. Manuf. 7 (4), 614–629. http://dx.doi.org/10.1016/j.ijlmm.2024.03.007.

Liu, P., Veitch, B., 2012. Design and optimization for strength and integrity of tidal turbine rotor blades. Energy 46 (1), 393–404. http://dx.doi.org/10.1016/j.energy.2012.08.011.

Lusty, A.F., Murdy, P., Gionet-Gonzales, J., 2024. Submerged Fatigue Testing of Marine Energy Advanced Materials. Technical Report, National Renewable Energy Laboratory (NREL), Golden, CO (United States).

MarkForged, 2020. MarkForged onyx filament datasheet, Rev. 5.3 ed. URL https://markforged.com/materials/plastics/onyx.

MarkForged, 2026. MarkForged ultem 9085 filament datasheet, Rev. 2A ed. URL https://markforged.com/materials/plastics/ultem-9085.

Marone, N., Barrington, M., Gunawan, B., McEntee, J., Wosnik, M., 2025. Performance of cross-flow turbines with varying blade materials and unsupported blade span. Renew. Energy 238, 121925. http://dx.doi.org/10.1016/j.renene.2024.121925.

Mouritz, A.P., Gellert, E., Burchill, P., Challis, K., 2001. Review of advanced composite structures for naval ships and submarines. Compos. Struct. 53 (1), 21–42. http://dx.doi.org/10.1016/S0263-8223(00)00175-6.

Murdy, P., Candon, C., Samborsky, D., Miller, D., Beach, R., 2024a. Polymer Additive Manufacturing for Marine Renewable Energy Applications: Best Practices, Research Trends, and Current Challenges. Technical Report, National Renewable Energy Laboratory (NREL), Golden, CO (United States).

Murdy, P., Lusty, A., Murray, R., Hughes, S., Beach, R., 2024b. Post-Deployment Characterization of Glass Fiber-Reinforced Thermoset and Thermoplastic Composite Tidal Turbine Blades. Technical Report, National Renewable Energy Laboratory (NREL), Golden, CO (United States).

Murdy, P., O'Dell, J., Barnes, D., McVey, J.R., Rumple, C., 2023. Investigating Marine Environmental Degradation of Additive Manufacturing Materials for Renewable Energy Applications. Technical Report, National Renewable Energy Laboratory (NREL), Golden, CO (United States).

Protolabs, 2026a. Inconel 3D printing. https://www.protolabs.com/services/3d-printing/direct-metal-laser-sintering/inconel/. (Accessed 27 May 2026).

Protolabs, 2026b. Titanium parts manufacturing. https://www.protolabs.com/materials/titanium/. (Accessed 27 May 2026).

Saini, G., Saini, R.P., 2019. A review on technology, configurations, and performance of cross-flow hydrokinetic turbines. Int. J. Energy Res. 43 (13), 6639–6679. http://dx.doi.org/10.1002/er.4625.

Siriruk, A., Penumadu, D., 2014. Degradation in fatigue behavior of carbon fiber–vinyl ester based composites due to sea environment. Compos. Part B: Eng. 61, 94–98. http://dx.doi.org/10.1016/j.compositesb.2014.01.030.

Snortland, A., Hunt, A., Williams, O., Polagye, B., 2025a. Influence of the downstream blade sweep on cross-flow turbine performance. J. Renew. Sustain. Energy 17 (1), 013301. http://dx.doi.org/10.1063/5.0230563.

Snortland, A., Van Ness, K., Franck, J.A., Athair, A., Williams, O., Polagye, B., 2025b. Experimental identification of blade-level forces, torque, and pitching moment for cross-flow turbines. J. Fluids Struct. 138, 104403. http://dx.doi.org/10.1016/j.jfluidstructs.2025.104403.

Stringer, C.C., Polagye, B.L., 2020. Implications of biofouling on cross-flow turbine performance. SN Appl. Sci. 2, 1–13. http://dx.doi.org/10.1007/s42452-020-2286-2.

Strom, B., Johnson, N., Polagye, B., 2018. Impact of blade mounting structures on cross-flow turbine performance. J. Renew. Sustain. Energy 10 (3), 034504. http://dx.doi.org/10.1063/1.5025322.

Villeneuve, T., Winckelmans, G., Dumas, G., 2021. Increasing the efficiency of vertical-axis turbines through improved blade support structures. Renew. Energy 169, 1386–1401. http://dx.doi.org/10.1016/j.renene.2021.01.092.

Wang, X., Travis, C., Sorna, M.T., Arola, D., 2024. Durability of Ultem 9085 in marine environments: A consideration in fused filament fabrication of structural components. Polymers 16 (3), 350. http://dx.doi.org/10.3390/polym16030350.